Insights into exhumation and mantle hydration processes at the Deep Galicia margin from a 3D high-resolution seismic velocity model

Bhargav Boddupalli[1*], Tim A. Minshull[1], Gaye Bayrakci[2], Gaël Lymer[3], Dirk Klaeschen[4] and Tim J. Reston[5]

[1]School of Ocean and Earth Science, University of Southampton, UK.

[2]National Oceanography Centre, Southampton, UK.

[3]School of Earth Sciences, University College Dublin, Ireland.

[4]GEOMAR, Helmholtz Centre for Ocean Research Kiel, Germany.

[5]School of Geography, Earth and Environmental Sciences, University of Birmingham, UK.

Abstract

High-resolution velocity models developed using full-waveform inversion (FWI) can image fine details of the nature and structure of the subsurface. Using a 3D FWI velocity model of hyper-thinned crust at the Deep Galicia Margin (DGM) west of Iberia, we constrain the nature of the crust at this margin by comparing its velocity structure with those in other similar tectonic settings. Velocities representative of both the upper and lower continental crust are present, but there is no clear evidence for distinct upper and lower crustal layers within the hyper-thinned crust. Our velocity model supports exhumation of the lower crust under the footwalls of fault blocks to accommodate the extension. We used our model to generate a serpentinization map for the uppermost mantle at the DGM, at a depth of 100 ms (~340m) below the S-reflector, a low-angle detachment that marks the base of the crust at this margin. We find a good alignment between serpentinized areas and the overlying major block bounding faults on our map, suggesting that those faults played an important role in transporting water to the upper mantle. Further, we observe a weak correlation between fault heaves and serpentinization beneath the hanging-wall blocks, indicating that serpentinization was controlled by a complex faulting during rifting. A good match between topographic highs of the S and local highly serpentinized areas of the mantle suggests that the morphology of the S was affected by the volume-increasing process of serpentinization and deformation of the overlying crust.

Plain Language Summary:

Continental rifting that occurred west of Iberia stretched and thinned the crust to less than 5 km thickness in the Deep Galicia Margin (DGM). We studied the nature of the thinned crust and upper mantle using seismic properties (P-wave velocities). Seismic velocities indicate that the thinned crust includes both upper and lower crust rocks. Velocities also suggest that the lower crustal rocks were exhumed along faults that cut through the entire crust to accommodate the stretching during the extension. Using seismic velocities, we generated a map showing the upper mantle hydration patterns below the thinned crust. The map shows a good alignment between the tips of the major crustal faults that reach the mantle and the mantle hydration pattern, suggesting that faults transported water to the mantle. Further, we find a weak correlation between fault heaves and serpentinization, suggesting that the hydration process is controlled by complex faulting during rifting. Our map indicates that the surface of the crust-mantle boundary (the S-reflector) was affected by the hydration process that caused volume expansion of the mantle rocks and also by the deformation of the crust that locally pulled up the mantle rocks.

1. Introduction

Rifting and breakup of the continents is a first-order tectonic process that results in the formation of new ocean basins and rifted margins. Significant spatial variations in the magnitude of extension, in the nature of the extended crust and in the degree of syn-rift magmatism arise along rifted margins. Accordingly, depending on the magmatic budget involved and identified in their distal zones, rifted margins are often termed as "magma-poor" and "magma-rich" (e.g., Franke, 2013), with a wide range of margin structures between these two end-members. The distal zones of magma-poor margins are commonly characterized by hyperextended crust associated with a complex network of extensional faults and with mantle exhumation preceding eventual continental breakup (Peron-Pinvidic et al., 2013). The mechanisms involved in the final stages of rifting are among the most debated aspects of rifting processes. Several different mechanisms have been proposed to explain the development and evolution of crustal hyperextension before continental breakup, involving the evolution and role of faulting and detachment faults in hyperextension, the development of asymmetry, and the nature and rheology of the crust and mantle during hyperextension (Brune et al., 2014; Ranero & Pérez-Gussinyé, 2010; Reston, 2005, 2009). It has been proposed that during the final stages of extension, embrittlement of the lower crust occurs progressively as the crust thins until the upper and lower crust become coupled and entirely brittle (Perez-Gussinye and Reston, 2001). Hyperextension is then accommodated by large normal faults that cut through the entire brittle crust and reach the underlying mantle (de Charpal et al., 1978; Lymer et al., 2019; Pérez-Gussinyé & Reston, 2001; Reston et al., 1996, 2007; Sibuet, 1992), with the faults acting as fluid conduits, transporting seawater to the upper mantle and resulting in its partial serpentinization (Bayrakci et al., 2016; Pérez-Gussinyé & Reston, 2001).

The Galicia Margin, west of Spain, is a sediment-starved, salt-free and magma-poor margin (Boillot & Winterer, 1988) that offers optimal conditions to study rifting processes from geophysical data (e.g., Hoffmann and Reston, 1992; Lymer et al., 2019). In particular, crustal hyperextension associated with reduced underlying mantle velocities, and exhumed serpentinized mantle, in the form of a Peridotite Ridge (PR) locally outcropping at the seafloor, were first observed at the Galicia margin (Boillot et al., 1980; Boillot & Winterer, 1988). Seismic imaging of the hyperextended zone of the Galicia Margin, known as the Deep Galicia Margin (DGM) (Figure 1), has revealed steeply dipping normal faults and tilted fault blocks overlying a narrow band of reflections collectively called the S-reflector (Boillot & Winterer, 1988; de Charpal et al., 1978; Reston et al., 1996, 2007). Crustal hyperextension in the DGM resulted in the development of extremely thinned and tightly coupled crust (< 5km) before the eventual crustal separation seawards (Pérez-Gussinyé & Reston, 2001).The extension has been explained by polyphase faulting (Reston, 2005; Reston & McDermott, 2014), or migrating faulting (Buck, 1988; Ranero & Pérez-Gussinyé, 2010) or a combination of both (Reston et al., 2007). In the polyphase faulting model the fault blocks bounded by normal faults are proposed to be rotated to low angles (<30°-Reston et al., 2007) until faults lock up and a new set of faults develop, possibly cutting through the

already existing faults (Reston, 2005; Reston & McDermott, 2014). In the migrating faulting models, the locus of extension migrates sequentially toward the future rift centre (Buck, 1988; Reston et al., 2007; Ranero & Pérez-Gussinyé, 2010), with a new fault forming in the hanging-wall of the previously active fault when the latter has rotated to low angle and locked-up, thus limiting cross-cutting to the distal root of the locked faults (Ranero & Pérez-Gussinyé, 2010).

One of the most intriguing questions is the evolution and role of the S-reflector of the DGM during crustal hyperextension. S has been interpreted variously as a brittle-ductile transition (de Charpel et al., 1978), as the crust-mantle boundary (Boillot et al., 1989) or, a detachment fault, either within the crust (Sibuet, 1992), at or near the crust-mantle boundary (Ranero & Pérez-Gussinyé, 2010; Reston et al., 1996, 2007). Slip of the overlying crustal fault blocks over along the S-reflector is inferred to have resulted in intense fracturing and brecciation in the lower parts of the crust (Reston et al., 1996). The presence of highly fractured rocks at the S-reflector level was inferred (Leythaeuser et al., 2005) , from one-dimensional (1D) full waveform inversion (FWI). The angular relationships between S and the overlaying faults and syn-rift packages suggest that slip on S occurred at angles as low as 20–25° (Lymer et al., 2019; Reston et al., 2007). Such low-angle slip requires very weak fault rocks such as serpentinite, and serpentinites were recovered at the DGM during Ocean Drilling Program (ODP) Leg 103 (Boillot et al., 1980; Boillot & Winterer, 1988). Serpentinization thus appears to be a fundamental process in the development of the S-reflector (Bayrakci et al., 2016; Liu et al., 2022; Lymer et al., 2019; Pérez-Gussinyé and Reston, 2001; Reston et al., 2007; Schuba et al., 2018), but the faulting mechanisms allowing ingress of water to the mantle and thus peridotite hydration and serpentinization are still debated.

In this study, we interpret the seismic velocity model of the DGM that was derived from 3D FWI applied to ocean bottom seismic data by Boddupalli et al. (2021). Based on this velocity model, we discuss the nature of the crystalline crust at the DGM (Figure 1) and present evidence for exhumation of the lower crust under the footwall of normal faults. We also present a serpentinization map generated 100 ms (~340 m) below the S-reflector. We then discuss the morphology of the S-reflector and how it is related to the normal faults based on our map.

2. Data and Method

Multichannel reflection and wide-angle seismic data were acquired at the DGM as part of the Galicia-3D (G3D) experiment in 2013 (Figure 1). The seismic signals were generated by two 3,300 cu.in arrays (each with 20 airguns) fired alternately at an interval of ~37.5 m. The signal was received by 6 km-long 480 channel streamers spaced 200 m apart, and 80 ocean bottom hydrophones/seismometers (OBS) deployed within the 3D survey area to record simultaneously wide-angle seismic data (Figure 1). The multichannel seismic volume was 3D pre-stack time-migrated over an area of 68.5 km (east-west) by 20 km (north-south). The wide-angle seismic data recorded by the OBSs (Bayrakci et al., 2022) were

used to generate a high-resolution velocity model using 3D full waveform inversion (FWI) (Boddupalli et al., 2021). The dimensions of the FWI grid were 78.5 km in the east-west direction by 22.1 km in the north-south direction (Figure 1; Boddupalli et al., 2021). The starting model for this FWI was obtained by 3D traveltime tomography (Bayrakci et al., 2016). The 3D FWI model was validated by recovering anomalies introduced into the starting model performing synthetic tests and by overlaying the velocity model on 3D seismic images (Boddupalli et al., 2021). Our interpretations are limited to the regions where the anomaly recovery tests were able to recover the anomalies without significant smearing (Supplementary Figures 1 and 2). The best resolution of a half wavelength at 5.2 Hz (maximum frequency used for inversion) corresponds to ~340m for 3.5 km/s, ~580 m for 6 km/s and ~675 m for 7 km/s, but the resolution may vary depending on the data coverage. Further details of the data and FWI method are given by Boddupalli et al. (2021).

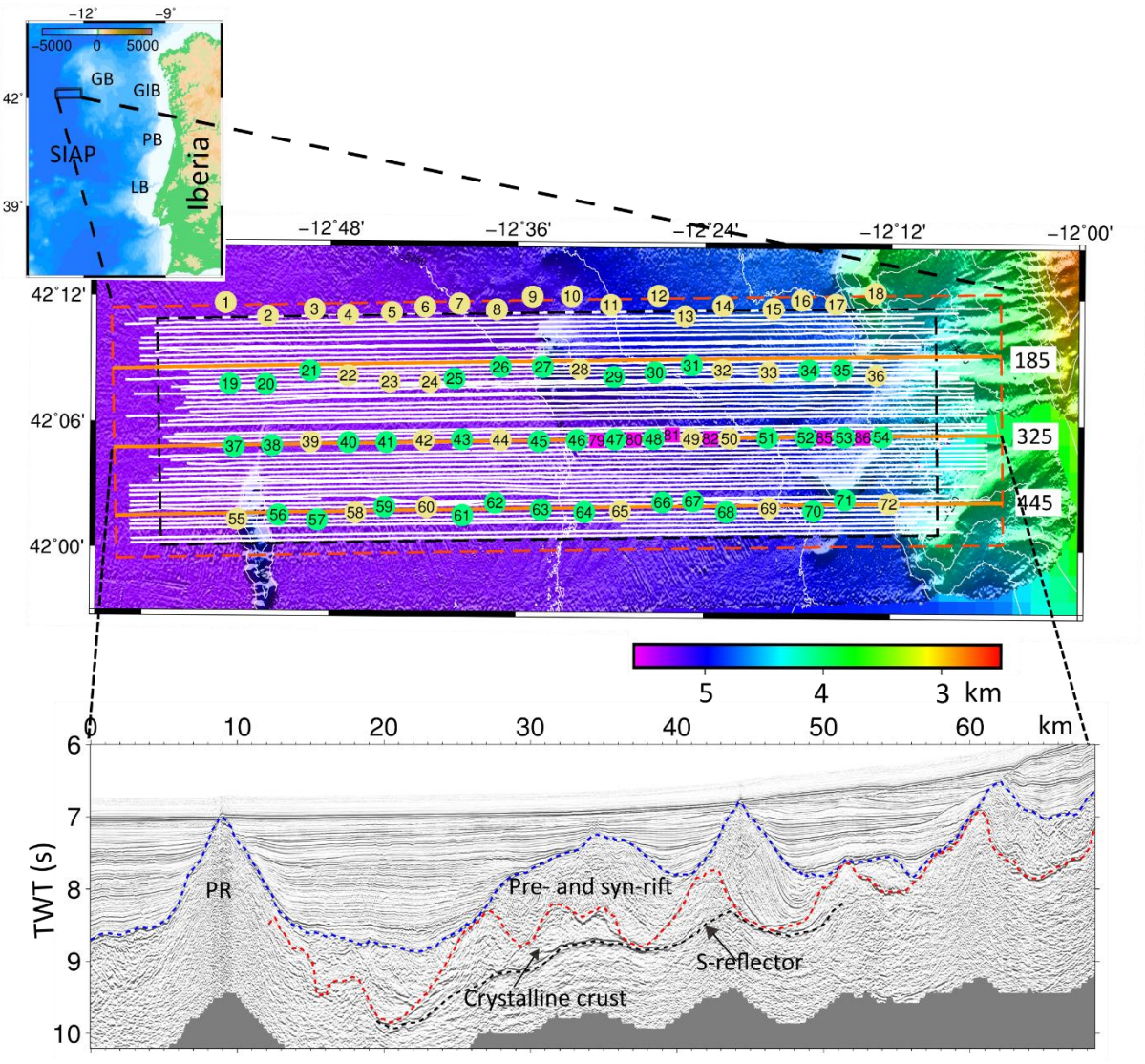

Figure 1| Bathymetric map of the DGM showing the location of the OBSs and seismic lines used in this study. The inset map shows the studied area (black box) west of Iberia. The dashed red box marks the area for the 3D FWI and the dashed black box marks the multichannel 3D seismic volume. The shot profiles recorded by the OBSs are shown in white lines. The orange numbered profiles mark the seismic-sections shown in Figures 5 and 6. Green circles mark OBS locations used for 3D FWI and yellow circle mark OBS locations that have not been used for FWI. The instruments in pink have only two shot profiles recorded directly above them and were used in full 3D FWI. GB, GIB, PB, LB and SIAP stand for Galicia Bank, Galicia Interior Basin, Porto Basin, Lusitanian Basin and Southern Iberian Abyssal Plain, respectively. Profiles 185, 325 and 445 shown in orange correspond to 700, 420 and 180 sections in the 3D time migrated seismic volume (Lymer et al., 2019). Bottom figure is the 3D time-migrated section along profile 325 highlighting different geological sections in the DGM; PR stands for Peridotite Ridge.

3. Results

The top of the crystalline crust in the time-migrated and depth-converted multichannel seismic volume varies between ~4.3 km and 10.7 km depth, generally increasing westwards (Figure 2a). In the 3D FWI model, the velocities at the top of the crystalline crust range between 5.7 and 1.5 km/s (Figure 2b); the latter occurs where crystalline basement reaches the seafloor and is the result of smoothing within a 200 m window of velocities across the seafloor. We calculated the thickness of the crystalline crust by subtracting this depth from the depth of the S-reflector (Figure 2d). Crustal thickness varies from 3.6 km, at the tops of faulted blocks, where the crust is the thickest to zero at the edges of some of these blocks (Figure 2). The mean velocity of the crystalline crust in the FWI model is 6.0 km/s (Figure 2e).

We extracted velocities from the 3D FWI model at the S-reflector and below the S-reflector using the S-reflector picked in two-way time by Lymer et al. (2019) and converted to depth using the 3D FWI velocities (Figure 3; Boddupalli et al. 2021). The depth of the S-reflector varies between ~7 and ~12 km. It is deeper in the south-west and shallower in the south-east and central north (Figure 3a). We conducted an anomaly recovery test in which synthetic dataset generated using the FWI model was used as observed data and inverted using the same starting model as the FWI (Boddupalli et al., 2021). The shapes of the anomalies were well recovered with little smearing, validating the anomalies introduced by 3D FWI (Boddupalli et al., 2021), but the amplitudes of the recovered anomalies are slightly lower than the actual anomalies (Supplementary Figure 1 & 2). Further validation of our velocity maps comes from a good match between the FWI model and multichannel seismic time slice at 9 s, which is the average time of the S reflector in the time-migrated seismic section (Supplementary Figure 3). The FWI model shows an abrupt lateral change in velocity that matches well the abrupt change in reflectivity that occurs at the S-reflector, indicating that the model has resolved well features at this depth (Supplementary Figure 3). In the FWI model, the mean velocity at the S-reflector is 6.7 km/s, which is higher than the mean velocity in the tomographic model of 6.5 km/s (Bayrakci et al., 2016). The FWI has introduced finer-scale velocity variations at the S-reflector that match the topography of the S-reflector (Figure 3a & 3b). Lower velocities would occur at topographic highs if the velocity increased

uniformly with depth, but this effect cannot be the cause of the correlation because the correlation is not present in the starting model (Figure 3c). In the 3D FWI model, the minimum and maximum velocities at the S-reflector averaged across a 100 m window, defined as the S-interval by Schuba et al. (2018), are 4.9 km/s and 8.2 km/s, respectively.

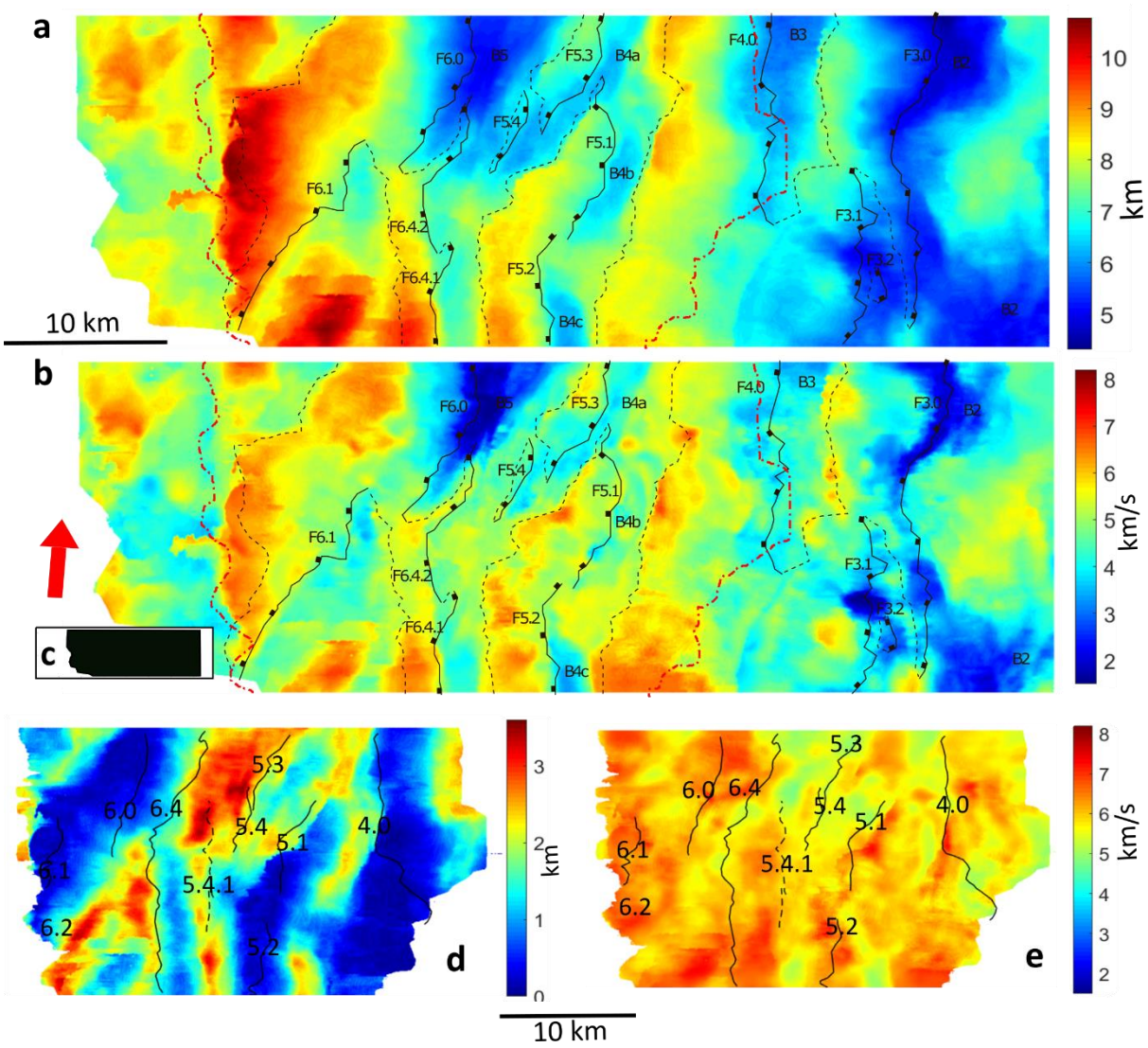

Figure 2| a) The top of the crystalline crust within the Galicia 3D volume (Lymer et al., 2019) converted to depth using the 3D FWI model (km) with faults (F-series) and fault blocks (B-series) numbered from Lymer et al. (2019). The footwall and hanging wall cut offs are marked as solid and dashed black line, respectively. Dashed dotted red lines show the extent of the S reflector; b) velocities along the top of the crystalline crust from the 3D FWI model with same markings and labels as in a; c) shows the location of these grids within the 3D FWI grid shown in Figure 1; d) thickness of the crystalline crust with fault intersections with the S-reflector in solid black lines. Fault 5.4.1 is plotted as dashed black line to indicate that it does not clearly cut (weak reflection) the S-reflector (see Supplementary Figure 5); e) mean velocity of the crystalline crust. The red arrow shows the north direction. Vertical scales are same as the horizontal scales. Upper scale bar is for a) and b) and lower scale bar is for d) and e).

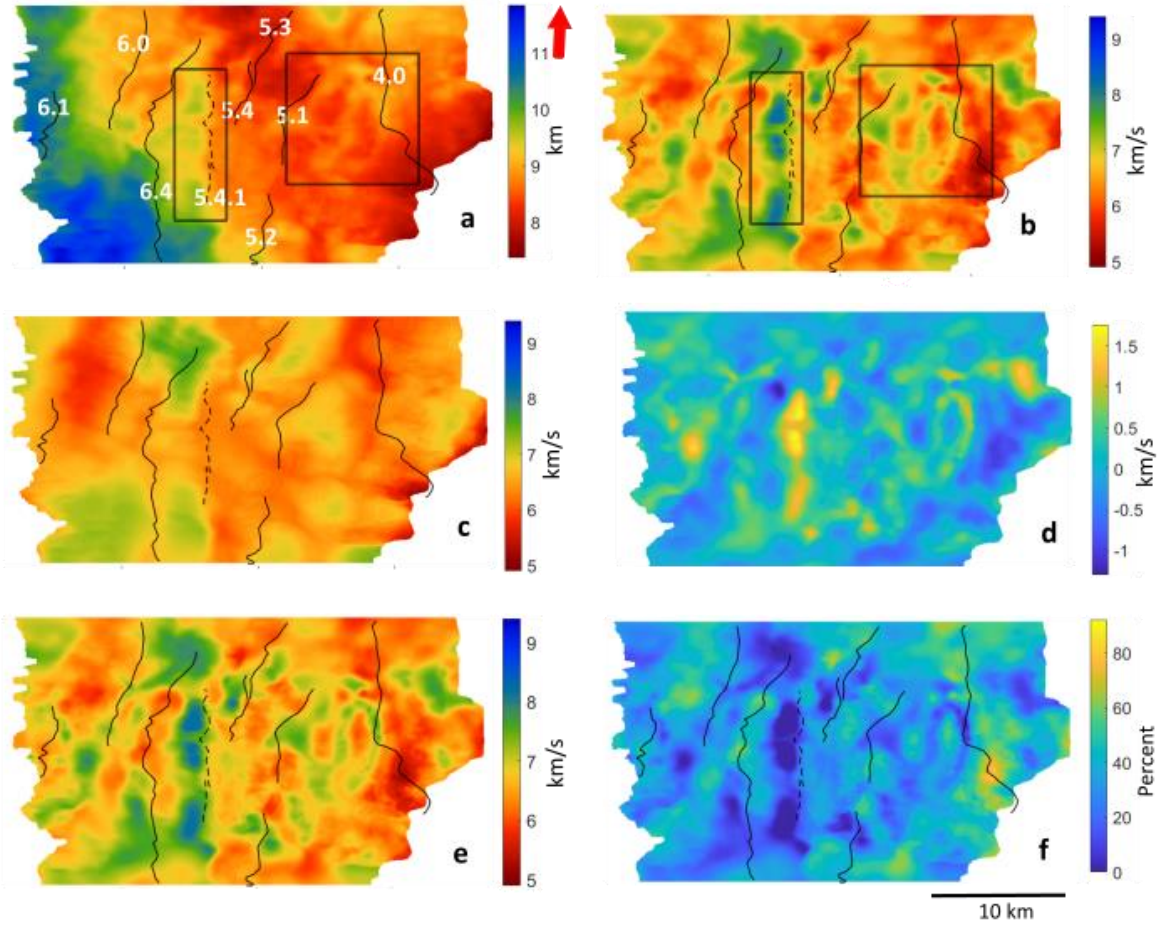

Figure 3| a) S-reflector map converted to depth using the 3D FWI model with fault intersections in solid black lines and their numbers in white (numbering after Lymer et al., 2019). Fault 5.4.1 is plotted as dashed black line to indicate that it does not clearly cut (weak reflection) the S-reflector. Solid black rectangles highlight the regions that show good correlation between the shapes on the S surface and the velocity map (b); b) velocities at the S-reflector from the 3D FWI model averaged over an interval of 100 m (S-interval; Schuba et al., 2018) across the S; c) velocities at the S-reflector from the 3D traveltime tomographic model of Bayrakci et al. (2016); d) difference between the 3D FWI and traveltime model at the S-reflector (km/s). e) velocities below the S-reflector averaged over an interval of 100 ms (~340 m) from the 3D FWI model; f) serpentinization map derived from velocities in e). The red arrow points to the north and the fault intersections from a) are also marked in b)-c) and e)-f)

Our velocity models along profiles close to the OBS locations show a good match with structural interpretations from the 3D pre-stack time-migrated multichannel seismic volume (Figures 4 and 5; Lymer et al., 2019). Lateral velocity variations within the sedimentary cover are less well recovered than those in the crystalline crust due to the sparse OBS spacing, and thus, not discussed here. Such variations are expected to be small and therefore have limited impact on our FWI results from the crust and uppermost mantle.

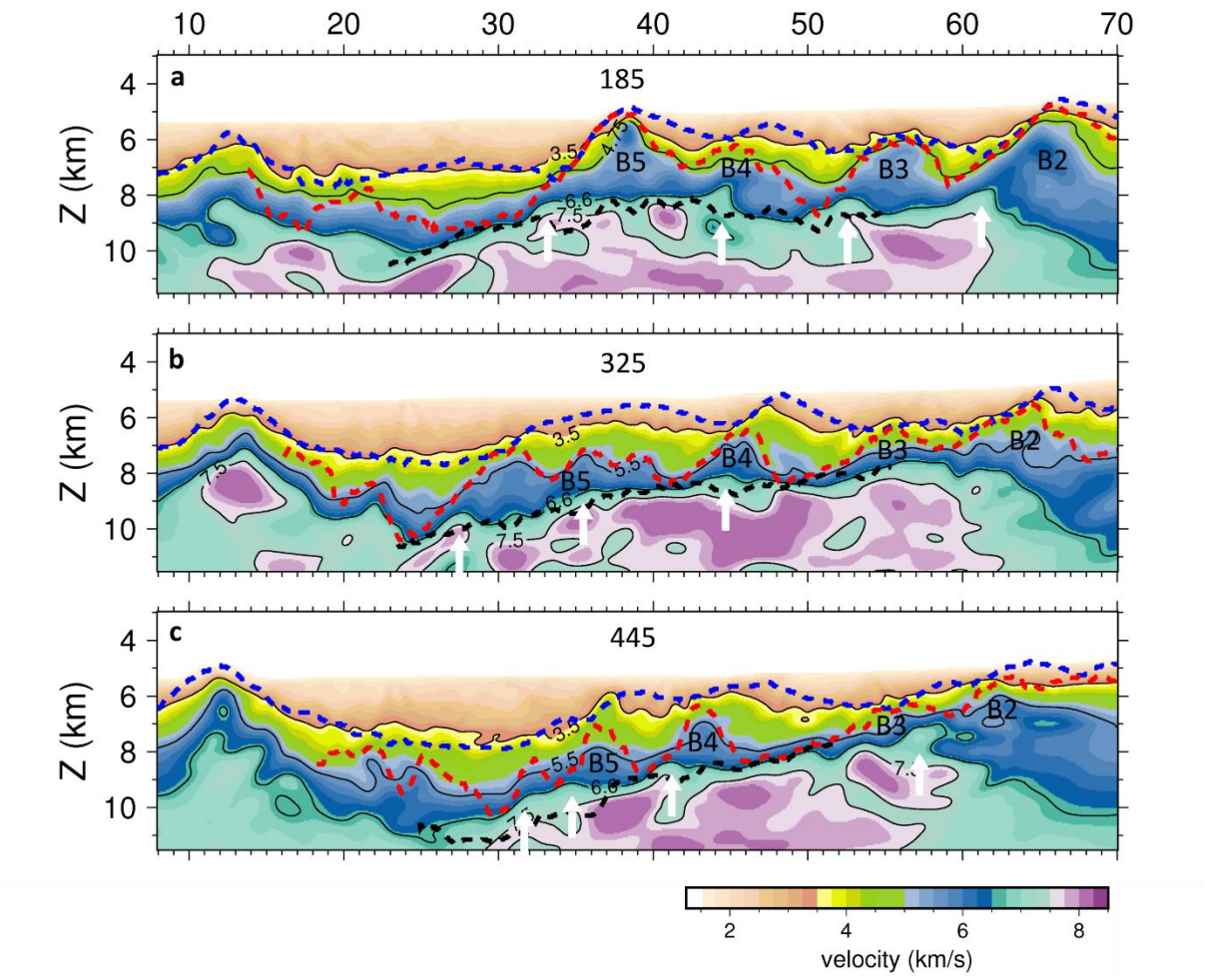

227

228 **Figure 4** | Velocity-depth sections along profiles 185 (a), 325 (b) and 445 (c) overlaid with
229 interpretations from the multichannel seismic volume. See Fig. 1 for locations. Dashed blue line
230 indicates the top of the syn-rift sediment, dashed red line indicates the top of the crystalline crust and
231 dashed black line indicates the S-reflector (Lymer et al., 2019). White arrows point towards the
232 shallowing of the 6.6 km/s velocity contour, which marks the top of the lower crust in the GIB (Pérez-
233 Gussinyé et al., 2003) (see text for detail). In the profile 325, the 5.25 km/s contour shows a good match
234 with the top of the crystalline crust. Fault block numbers (B-series) are from Lymer et al. (2019).

235

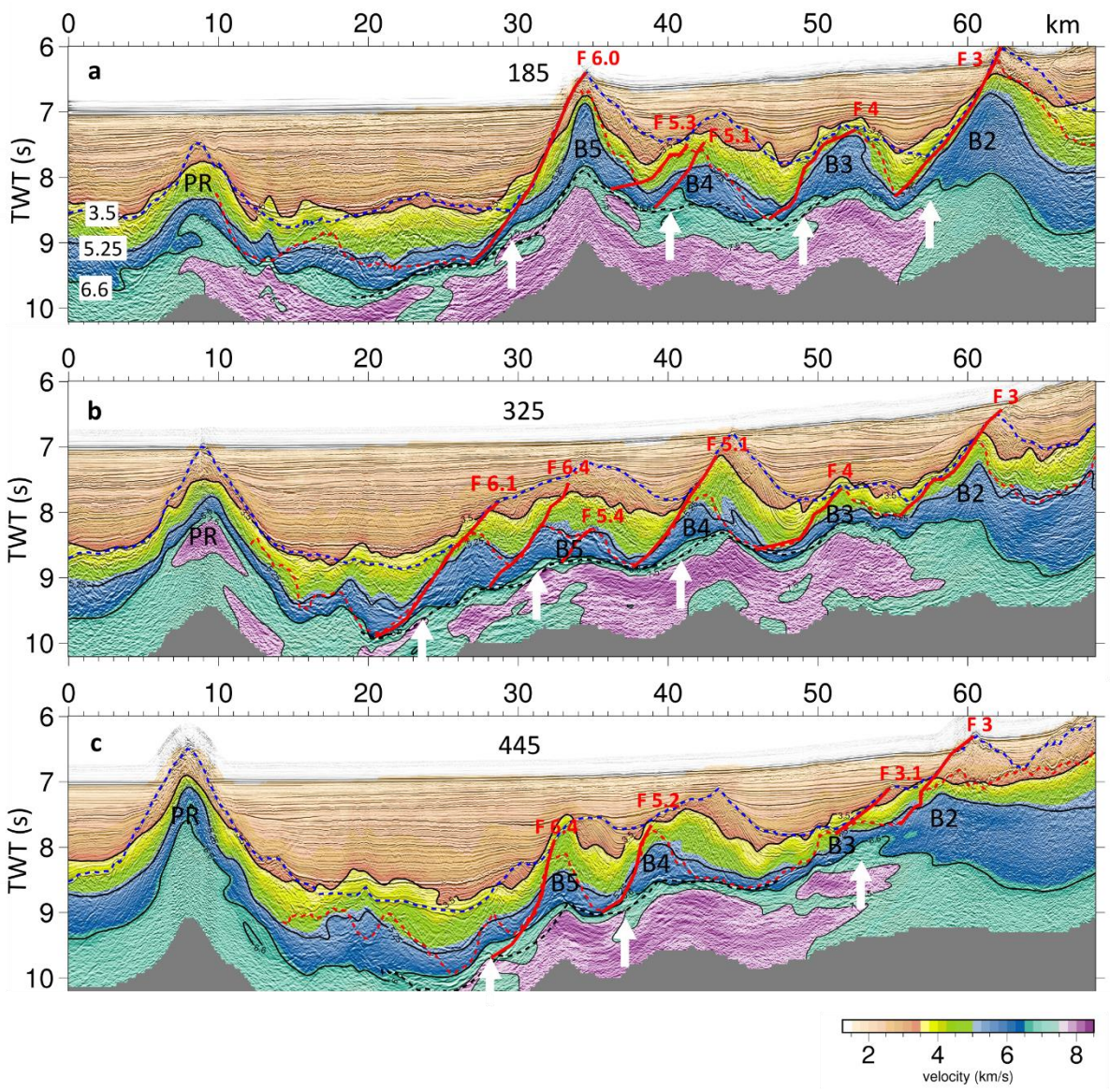

Figure 5 | Time-converted velocity sections overlaid on 3D multichannel seismic images along profiles 185 (a), 325 (b) and 445 (c) in two-way-time (s) with interpretations. Dashed blue line indicates the top of the syn-rift sediment, dashed red line indicates the top of the crystalline crust and dashed black line indicates the S-reflector (Lymer et al., 2019). Thick red lines indicate the block bounding faults. White arrows point towards the regions where the velocity contour of 6.6 km/s shallows. Velocity contours as solid black lines are as in Figure 4. Fault block numbers (B-series) from Lymer et al. (2019).

4. Discussion

4.1 Nature of the crystalline crust

Here we discuss the nature of the crust in the DGM based on the velocities derived from the 3D FWI and compare our results with the velocity models from other similar tectonic settings.

In locations where the thickness of the crystalline crust is less than 2 km, the velocity tends to be around 6 km/s and higher, while in the locations where the crust is thicker, the velocity varies between ~4.8 km/s and ~6.7 km/s (the velocity at the S-reflector). The mean velocity of the crystalline crust in the

DGM is 6.0 ± 0.4 km/s (Figure 2), which is less than (but within error of) the global velocity average of the continental crust, including velocity models from diverse tectonic settings, of 6.5 ± 0.21 km/s (Christensen & Mooney, 1995). However, the mean velocity is also close to the global means at 10 km depth for extended crust (6.0 ± 0.2 km/s) and rifts (6.0 ± 0.1 km/s) (Christensen & Mooney, 1995). These global averages do not include velocity models from hyperextended zones. The velocity limits of the crystalline crust in the DGM agree well with those of thinned continental crust in the northern part of the Southern Iberian Abyssal Plain (SIAP; Figure 1) where the velocity ranges between 5.0 and 6.6 km/s (Chian et al., 1999). This comparison is appropriate because the thickness of the hyper-extended crystalline crust in the SIAP is in the same range (2-5 km) as in the DGM, and the northernmost line of Chian et al. (1999) is only ~170 km from the southern limit of our study area. Another interesting comparison is with crustal velocities in the Galicia Interior Basin (GIB; Figure 1) immediately landward of the DGM, which provide insights into earlier stages of extension of the lithosphere. In the centre of the GIB, the crystalline crust thickness is ~7-8 km, with the upper and lower crust identified as distinct layers (Pérez-Gussinyé et al., 2003). The velocity limits for the upper and lower crust obtained from wide-angle seismic data in the GIB are 5.3-6.4 and 6.6-6.9 km/s, respectively (Pérez-Gussinyé et al., 2003). These limits together encompass the velocity limits of the crystalline crust in the DGM, suggesting that this crust is composed of both upper and lower crustal rocks. In addition, recovery of lower crustal rocks from drilling in the neighbouring SIAP (Whitmarsh et al., 2000) further supports the possibility of presence of both upper and lower crustal rocks in the DGM. Measurements on the lower crustal cores showed velocities between 4.9-6.6 km/s with a modal velocity of ~5.7 km/s (Whitmarsh et al., 2000), which is within the limits of the crustal velocities observed in the DGM.

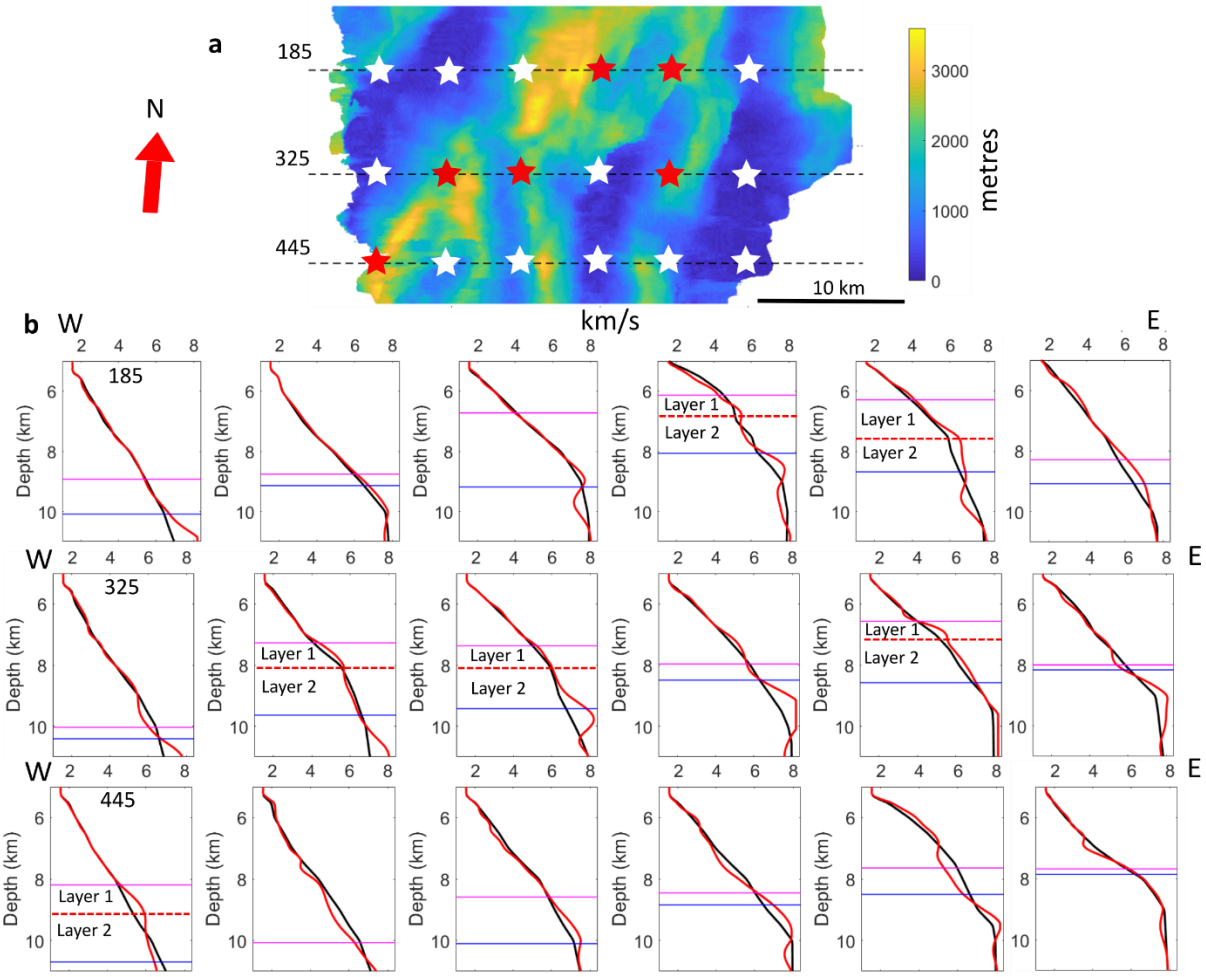

Figure 6 | a) Crystalline crust thickness calculated between the top basement and S surfaces, with white and red stars showing the locations of the 1D velocity profiles extracted from the 3D FWI model along profiles 185, 325 and 445. Red stars indicate the locations where we observe two layers within the crystalline crust; b) 1D velocity profiles from the starting (black) and 3D FWI model (red) with profile location following the same order as the order of the stars on the profiles. Pink and violet colours in each profile mark the top of the crystalline crust and S-reflector depths, respectively. The dashed red line indicates the boundary between two distinct layers within the crystalline crust.

In a few locations, the crystalline crust can be divided into a higher-gradient upper part and a lower-gradient lower part (Figure 6). To investigate further this subdivision, velocity profiles were plotted every 1 km between 25 and 35 km along profile 325 across one fault block (Figure 7). Here it can be observed that as the crystalline crust thickens, the 1D velocity profiles show two layers with different velocity gradients. This layering is only observed where the thickness of the crystalline crust is greater than ~2 km (Figure 6). It is possible that such layering might be present also where the crust is thinner, but is not resolved in our model. We note that structural interpretation of the 3D volume did not identify continuous layering within the crystalline basement or below S across the DGM (Lymer et al., 2019). The upper layer (Layer 1 on Figure 7) has a higher velocity gradient (0.2-0.3 s^{-1}) with the velocity ranging between ~4.8 and 5.3 km/s, and the lower layer (Layer 2) shows velocity range between ~5.3 and 6.7 km/s with a lower velocity gradient (Figure 7). The velocity ranges of these layers vary along

and across the volume. Layer 1 marks the top of the crystalline crust and its high gradient and low velocities are inferred to result from fracturing and related mechanisms, as in the GIB and the Porcupine basin (Pérez-Gussinyé et al., 2003; Watremez et al., 2018). Layer 1 thickens towards the centre of fault block number B5 where the crust is thickest (Figure 7), perhaps indicating that fracturing processes were mainly active over the top of the fault blocks. Moreover, this zone correlates well with a previous interpretation from seismic reflection images that the crests of fault blocks were flattened as a result of mass wasting or subaerial erosion during rifting (Reston et al., 2005, 2007).

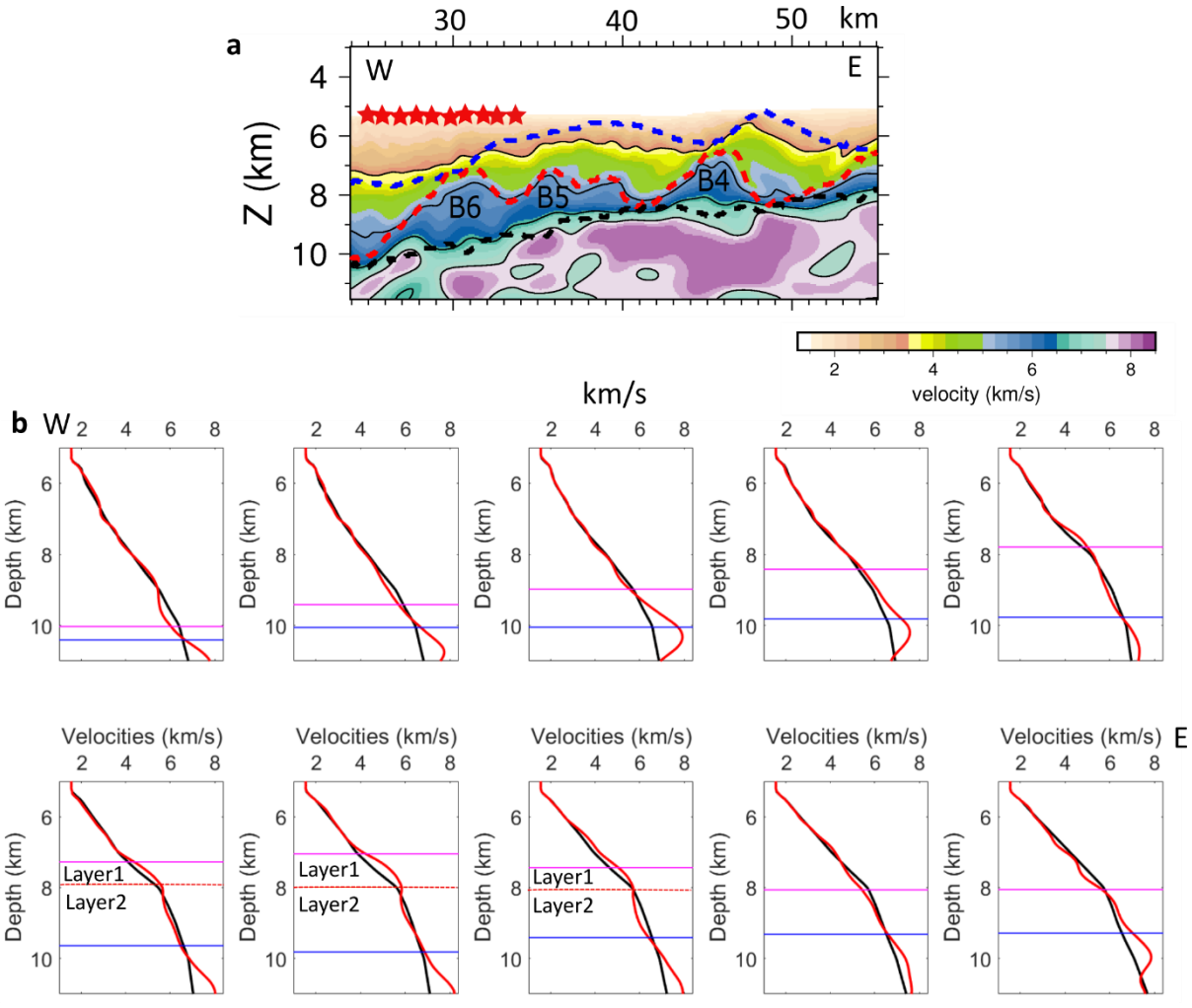

Figure 7 | a) Red stars indicate the locations of the 1D velocity profiles shown in (b) between 25 and 35 km (west to east) on the velocity profile 325 with interpretations as in figure 4 b) 1D velocity profiles from the 3D FWI model at the locations indicated by the red stars in (a). As the crustal thickness increases towards block number B6 in the west, the 1D velocity model shows two distinct crustal layers.

4.2 Exhumation of the lower crust

Final exhumation to the surface must always be brittle (except for lava) as all rocks are brittle at the low pressures and temperatures of the shallow sub-surface. As the crust thins during extension, the upper and lower crust become tightly coupled and increasingly brittle until the whole crust is completely brittle (Pérez-Gussinyé & Reston, 2001) preventing such flow, so that continued exhumation is likely

to be along brittle faults. However, some thermo-mechanical models predict that hot, ductile lower crust may be partially exhumed by flowing locally along an "exhumation channel" beneath the footwall of the active normal faults (Brune et al., 2014, 2017), and even that such ductile flow can continue into the final stages of extension (Liu et al., 2022). Our 3D FWI model of the DGM is consistent with the exhumation of the lower crust rocks: if we consider the 6.6 km/s velocity contour as the top of the lower crust from the GIB (Pérez-Gussinyé et al., 2003), it shallows under the footwall of the faults (Figure 4 and 5). Although the undulations on the 6.6 km/s contour in a few locations are small, there are locations where the velocity perturbations rise up to 1 km above the S-reflector beneath the footwall of the normal faults (Figure 4 and 5). These velocities match both the ranges of velocities for serpentinites and for lower-crust, but it is unlikely that mantle rocks were exhumed to nearly 1 km above the S-reflector, so we favour the local presence of lower crust there.

Additional support that the 6.6 km/s slivers just above S within the western tip of the footwall blocks might be lower crustal rocks comes from the ODP data of the SIAP (Whitmarsh et al., 2000), where lower crustal rocks were cored on top of a basement high (ODP Sites 1068 and 900) adjacent to serpentinites seaward (ODP Site 1067) separated by a detachment fault, the H-reflector (Krawczyk et al., 1996). In the SIAP, where the hyperextended crust is similar to the DGM, it is suggested that a small lens of the lower crustal rocks at the top of a basement high was exhumed from a deeper depth where an originally steep seaward-dipping normal fault that now forms the western flank of the 900 fault block cuts across the H reflector (Krawczyk et al., 1996; Whitmarsh et al., 2000). This fault lies in exactly the same depth range where we observe the 6.6 km/s slices above S in the DGM, which may thus similarly indicate the presence of lower crust. Lower crustal exhumation forms a component of all the lithospheric extension mechanisms that are proposed for the final stages of rifting: the polyphase model and migrating faulting model (Buck, 1988; Lymer et al., 2019; Ranero & Pérez-Gussinyé, 2010; Reston, 2005).

4.3 Velocities at and below the S-reflector

The velocity pattern at the S-reflector shows a good correspondence with the topography of the S-surface and with the location of fault intersections (Figure 3). The deep and shallow features correlate with locally high and low velocities, respectively (Figure 3). It is challenging to differentiate crustal and upper mantle rocks using only P-wave seismic velocities because serpentinized upper mantle rocks can show a wide-range of velocities (~5-8.3 km/s for intact rock), depending on the degree of serpentinization, spanning the velocity limits of crystalline crust (Christensen, 2004). In the central region, the model shows high velocities (> 8 km/s) indicating the presence of unaltered peridotites there (Figure 3b & 3e). These high-velocity locations may have higher uncertainties in the velocity due to the significant anisotropy that can be associated with unaltered peridotites (Christensen, 2004), that is not accounted for in our inversion (Boddupalli et al., 2021). In a few locations the velocity reaches 8.2

km/s, which was set as the maximum velocity allowed in the inversion (Boddupalli et al., 2021). However, the anomaly restoration test supports the presence of these high velocities (Supplementary Figure 1). Based on seismic images and high-resolution velocity models, the lower regions of the crystalline crust in the vicinity of the S-reflector have been interpreted as fractured and brecciated serpentinized peridotites and/or crustal rocks (Leythäuser et al. 2005; Reston et al., 1996; Schuba et al. 2018); although some numerical simulations of hyperextension generate fragments of lower crust below S (Liu et al., 2022), as discussed above the detailed internal structure of the S-interval as identified by Leythäuser et al. (2005) and Schuba et al. (2018) is beyond the resolution of our 3D inversion strategy (Boddupalli et al., 2021). However, we do locally identify slivers of lower crust sandwiched between the S and the faults that detach onto S (Figure 4). The 3D FWI velocity model closely matches with the multichannel seismic image time slice sections at the mean S-reflector depth (Supplementary Figure 3; Boddupalli et al., 2021), giving confidence in the velocities at this depth.

4.4 Serpentinization and relationship with faulting

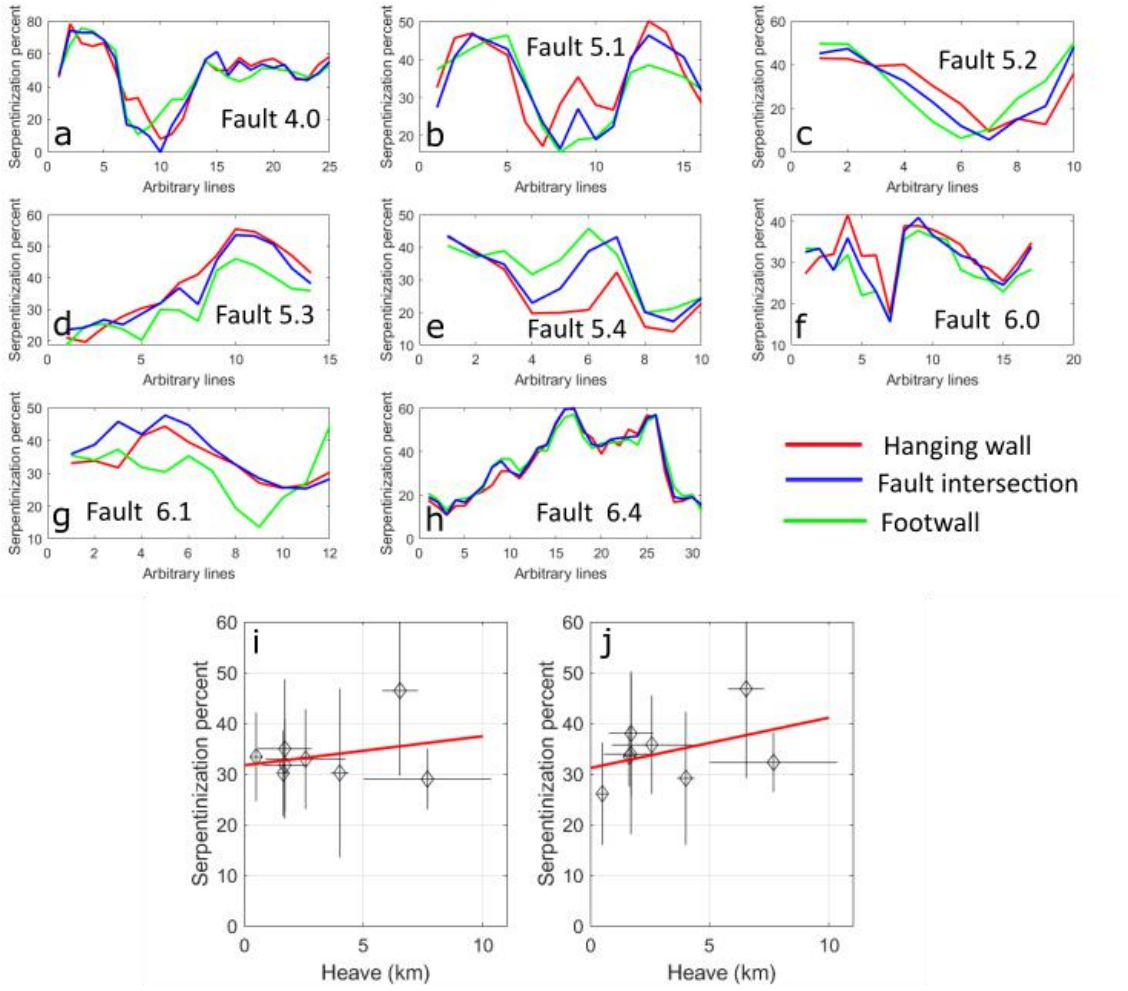

359

360 Figure 8 | a)-h) Serpentinization estimates averaged over a length of 1 km along the arbitrary lines from
361 the point of fault intersection (blue) in the hanging wall (red) and footwall (green) directions for each
362 fault intersection. The x-axis represents number of arbitrary lines intersected by fault intersections from
363 south to north (Supplementary Figure 4). i)-j) Correlation plot between the average fault heave and
364 serpentinization percent under foot wall (i; R-squared: 0.08) and hanging wall blocks (j; R-squared:
365 0.2). The diamonds represent each fault plotted at their average heave and serpentinization values. The
366 error bars on the diamonds indicate one standard deviation. The red solid lines represent a linear fit
367 between the points.

368

369 The overall alignment between the variation in the degree of serpentinization (colours in Figure 3f) and
370 the line of intersection of the overlying faults with S (black lines in Figure 3f) indicates that these faults
371 played an important role in transporting water to the mantle (Figure 3f). The match is particularly good
372 for the northern parts of faults 4.0 and 5.1 and for most of faults 5.3, 6.4 and 6.0, all of which reach the
373 mantle and thus provide viable fluid pathway for serpentinization. To further investigate the variations
374 in serpentinization across the fault intersections with S, we plotted mean serpentinization under the
375 footwall and the hanging wall for each fault along with the serpentinization values at the fault
376 intersection (Figure 8). The mean curves are calculated over a length of 1 km from the fault intersections
377 in the footwall and hanging directions along a series of arbitrary lines (Supplementary Figure 4) in the

direction of the corrugations observed in the 3D reflection volume as defined by Lymer et al. (2019) (Figure 8). Some of the fault intersections display higher serpentinization values under hanging wall side than footwall side across major part of their intersection with the S. These include fault 6.0, shown from structural interpretation to be one of the faults of the DGM with the largest offset and best developed corrugations (Lymer et al., 2019), suggesting that serpentinization may have facilitated slip at low angle along this fault. However, at other fault intersections such as 5.4 and 6.4 (southern segment, Figure 3f), low serpentinization occurs toward the hanging wall side. These areas of low serpentinization may be due to changes in the water supply along the faults resulting from factors, such as fault permeability, fault connectivity, and transfer of activity from one fault to another during hyperextension. In the central region, the alignment of the fault intersection 5.4.1 on the eastern edge of an area of limited serpentinization (Figure 3f) suggests that very little or no water reached the mantle along this fault, probably because fault 5.4.1 does not appear to reach the S-reflector on the vertical sections of the 3D seismic volume, e.g., between 30 and 40 km along profile 325 (Supplementary Figure 5).

The variations in the degree of serpentinization below S evidenced by our map of serpentinization (Figures 3f and 9) also suggest that there was little or no flow of water along the entire length of S from the proximal to the distal DGM as might have been expected if S was one single structure active simultaneously everywhere. But it should be noted that the depth-migrated seismic sections showing that the gradient along S might have been too low to generate sufficient pressure difference for water to flow (Supplementary Figure 6; Ranero & Pérez-Gussinyé, 2010). The lack of lateral continuity in serpentinization in the EW transport direction is consistent with previous suggestions that the S-reflector consists of the root zone of individual block bounding faults that linked and merged while rotating to low angles (Lymer et al., 2019; Ranero and Pérez-Gussinyé, 2010; Reston et al., 2007): there was never a single EW extensive active detachment but rather a succession of NS oriented faults. In summary we conclude that water along S was not transported horizontally along S, but mainly through the steeper overlying faults and associated fault blocks, and distributed heterogeneously parallel to those faults.

Bayrakci et al. (2016) established a strong positive correlation between the average fault heaves for individual faults and degree of serpentinization beneath the hanging wall. However, that study only used fault interpretations along three 2D seismic profiles from the DGM. We have revisited this correlation using the fault heaves obtained from the 3D seismic volume (Lymer et al., 2019). As these measurements exhibit a lot of scatter (Supplementary Figure 7). We adopt an averaging approach to capture the general trend. Our approach differs from that of Bayrakci et al. (2016), in which the degree of serpentinization was averaged over a window of 7 km laterally and 2.5 km vertically below S along 2D seismic lines for each normal fault intersecting S. In this study, we calculated the mean degree of serpentinization related to each normal fault from the serpentinization map (Figure 3f) by averaging the degree of serpentinization within 1 km along the arbitrary lines and along the fault intersections with S

(Figure 8; Supplementary Figure 3). The FWI serpentinization map is averaged over 100 ms (~340 m) vertically and we calculated the mean degree of serpentinization for each fault on either side of the fault intersection (hanging wall and footwall sides; Figure 8). Thus, our mean serpentinization values for each fault are averaged 100 ms vertically, 1 km along the arbitrary lines on the hanging wall and footwall sides of each fault intersection, and along the fault intersections (Figure 3f; Supplementary Figure 4).

In contrast to Bayrakci et al. (2016), we find only a weak correlation between the mean fault heaves and degree of serpentinization below the hanging wall (Figure 8). Our approach included more data points from the complete 3D seismic volume (Lymer et al., 2019) into the fit than Bayrakci et al. (2016) and estimated serpentinization in the direction of extension using a high-resolution velocity model (Boddupalli et al., 2021). It is possible that this approach has highlighted the contribution of additional processes of transport of water that affected the water transportation process to the mantle during hyper-extension, resulting in the weak correlation (Figure 8). Numerical modelling of mantle hydration at mid-ocean ridges and oceanic transform faults suggested that serpentinization of the upper mantle is affected by brittle crustal deformation, spreading rate, slip rate of faults, and fault length (Rüpke & Hasenclever, 2017). Such studies are missing at rifted margins but similar factors may have controlled serpentinization at the DGM. The interplay between these different factors tends to be complex, especially in the final stages of rifting when crustal deformation is accommodated by complex faulting that weakens the correlation between serpentinization and the heaves of the current block-bounding faults that form the S-surface. It is also possible that the volume that we use for averaging is not fully representative of the serpentinization beneath S at a given location.

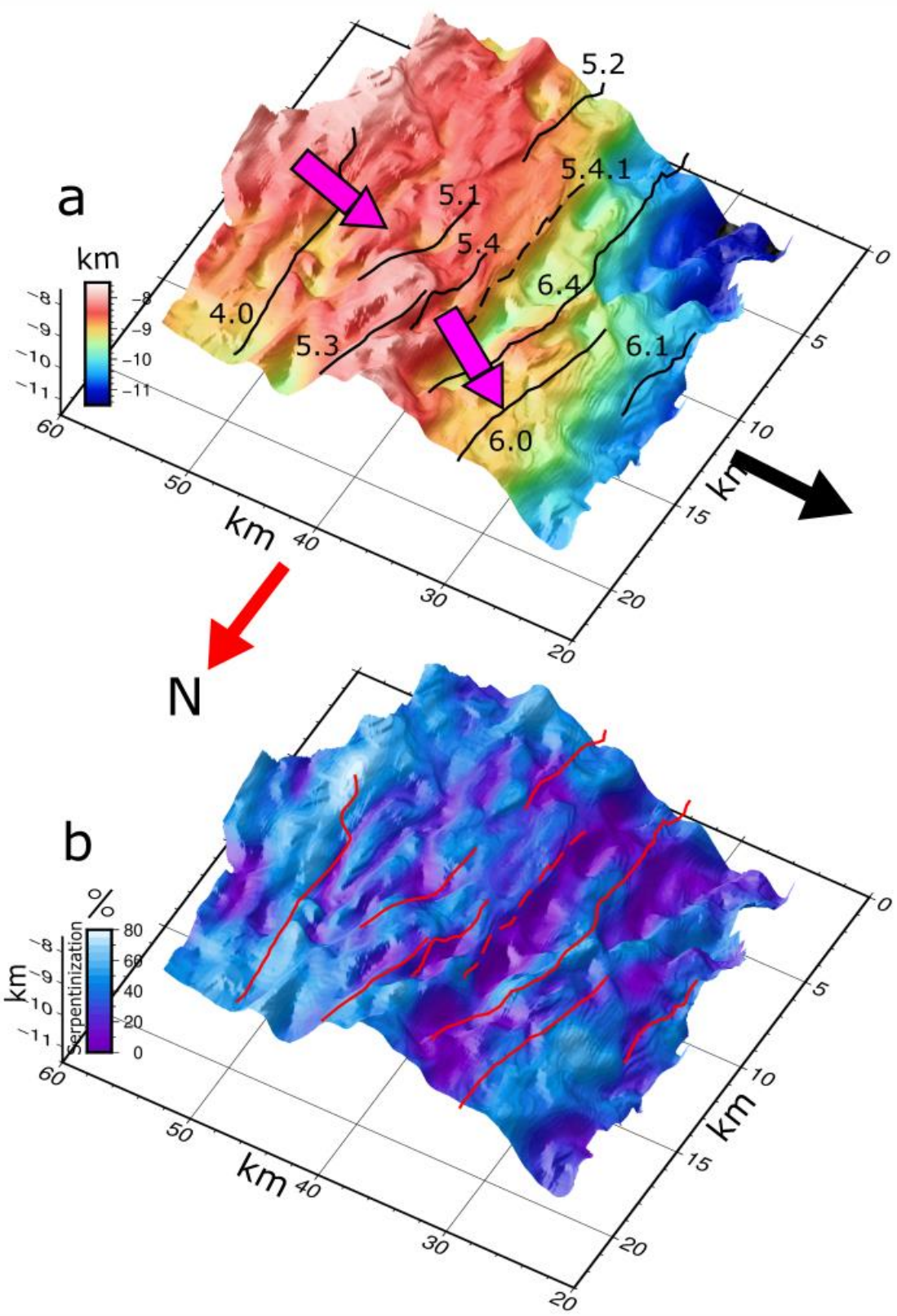

Figure 9| . The top figure (a) shows depth variation of the S surface in 3D with fault intersection marked in solid black lines except for fault 5.4.1, which is marked as a dashed line. Magenta arrows mark the corrugation direction, black arrow points toward the deeper sea and red arrow points in the north direction. The bottom figure (b) is the perspective view of the S reflector in the same orientation as in the top figure, with colour scale showing serpentinization percentage of the upper mantle (~340 m

below S) and fault intersections marked in red. The z-axis is depth in km with deeper features (topographic highs) showing lower serpentinization. Horizontal axes are same as in figure 3.

4.5 S-surface morphology

The pattern of serpentinization shows a good correlation with the topography of the S-reflector with deeper features showing lower serpentinization locally (Figure 9). Such a correlation between high-relief on S and serpentinized area suggests a relationship between the morphology of the S and serpentinization process. Perhaps the morphology of S may be attributed, at least in part, to the change in volume resulting from serpentinization (Graham, 1917), especially given the heterogeneous serpentinization pattern that we evidence (Figure 9). Serpentinization can increase the volume of the rocks by ~40 %, and such a large increase could result in changes in the structure of a bounding surface due to buoyancy (Germanovich et al. 2012; Lister, 1974) as well as by simple vertical expansion. In either case, the serpentinization process may have affected the topography of the S-surface by uplifting the overlying thin crustal section. This correlation is also consistent with our attribution of the velocity reduction in the uppermost mantle primarily to serpentinization, and inconsistent with the idea that the velocity reduction is due to residual fracture porosity (Korenaga, 2017).

The normal faults intersect the top of S at local highs implying that tectonic deformation also played an important role in shaping the S surface. In a tightly coupled system (Lymer et al., 2019; Perez-Gussinye & Reston, 2001) uplift of the faults' footwall could directly include the serpentinizing mantle (pulling up the mantle rocks which are undergoing serpentinization), but even if coupling was restricted to the crust once the underlying mantle was weakened by serpentinization, the uplift would create the space beneath the footwall into which weak serpentinites might flow. We suspect that both processes occurred to some extent. The effect is apparent along the fault intersection 6.4 which forms a ridge of serpentinites between two low lying areas on either side (Figure 9). However, the uplift of S is not transmitted through the crust as there is no correlation between the depth of S and either the top of the crystalline crust (Figure 2a and 3a), or the base of the postrift section (top of the faulted layer – Lymer et al., 2019). Given our understanding that serpentinization was not present before rifting (e.g., Bayrakci et al., 2016), this lack of correlation suggests that the uplift and hence the serpentinization occurred during rifting when the faults were tectonically active and transported water to the mantle serpentinizing it.

The depth of the S-reflector changes drastically from south to north seawards beyond the fault intersection 6.4, with deeper reflections in the south (Figure 9). This change roughly coincides with the change in the direction of rifting from E-W to ESE-WNW seawards of the fault intersection 6.4 (magenta arrows in Figure 9a) deduced from the orientation of corrugations observed on the S surface in the 3D migrated seismic volume (Lymer et al., 2019; Schuba et al., 2018). This observation suggests that the direction change of rifting might have affected the dynamics of extension in the south and north differently, thereby the large-scale morphology of the S (Figure 9). Our images indicate that the

serpentinization process, crustal deformation, and rifting direction controlled the S surface's morphology. However, contributions from other parameters like lithosphere strength, speed of extension, and rift obliquity cannot be ignored. The interactions between different controlling parameters and feedback between them make it extremely difficult to study their individual influence on the development of the S (Brune, 2016; Peron-Pinvidic et al., 2019).

5. Conclusions

We have presented a 3D FWI model along three profiles 185, 325 and 445 oriented in the East-West direction and discussed the nature of the hyperextended crust and exhumation of the lower crust during the late stages of extension at the DGM. We have explored variations in velocity at the top of the crystalline crust, the S-reflector and in the mantle at 100 ms depth below the S-reflector. Based on our results, we conclude the following:

1. The mean velocity of the crystalline crust in the DGM (~ 6 km/s) matches closely with global averages at a depth of 10 km in extended continental crust. The velocities in the crystalline crust vary between ~4.75 and 6.7 km/s, matching closely those observed in the neighbouring SIAP and GIB. Within the crystalline crust, we find little evidence for distinct upper and lower crustal layers.
2. At the top of the crystalline crust a layer with a high velocity gradient is identified where the crystalline crust thickness is greater than 2 km, that we attribute to fracturing and related mechanisms at the top of the crystalline crust.
3. The 6.6 km/s velocity contour shallows under the footwall of the overlying normal faults, consistent with local exhumation of the lower crust under the footwall of the normal faults to accommodate extension.
4. A good alignment between the serpentinization areas and block bounding fault intersections support the idea that faults played a key role in transporting the water to the upper mantle. However, a weak correlation between the degree of serpentinization and fault heaves suggests that fault permeability is controlled also by other factors.
5. Water transport was controlled by the overlying active faults, which rotated to low angles during extension, but lateral water transport along the S reflector was limited. Lack of correlation between the S-surface morphology, the top of the crystalline crust and the base of the post-rift sediment suggests serpentinization occurred before deposition of the post-rift.
6. A good match between the velocity variations just below the S-reflector and the topography of S may be attributed to variable buoyancy of serpentinite and to deformation in the overlying crust.

Data Availability

The multichannel seismic data set used for this study can be found online (https://doi.org/10.1594/IEDA/500151). The OBS data underlying this paper can be found at https://doi.pangaea.de/10.1594/PANGAEA.940656.

Acknowledgements

Data acquisition was supported by the U.S. National Science Foundation (grant OCE-257 1031769), the UK Natural Environment Research Council (NERC; grant NE/E016502/1 and NE/E015883/1), and GEOMAR. Ocean bottom instrumentation was provided by the NERC UK Ocean Bottom Instrumentation Facility (Minshull et al. 2005) and by GEOMAR. We thank Joanna Morgan, Imperial College London, for assisting us with 3D full waveform inversion. We acknowledge the use of the IRIDIS High Performance Computing Facility, and associated support services at the University of Southampton, in the completion of this work. The 3-D ProMAX/SeisSpace package, supplied by Halliburton under a university software grant, was used to preprocess and analyse the field data within University of Southampton. We thank two anonymous reviewers and the associate editor whose comments improved the manuscript.

References

Bayrakci, G., Minshull, T. A., Sawyer, D. S., Reston, T. J., Klaeschen, D., Papenberg, C., et al. (2016). Fault-controlled hydration of the upper mantle during continental rifting. *Nature Geoscience*, *9*(5), 384–388. https://doi.org/10.1038/ngeo2671

Bayrakci, Gaye; Minshull, Tim A; Boddupalli, Bhargav; Davy, Richard G; Klaeschen, Dirk; Papenberg, Cord; Sawyer, Dale S; Reston, Timothy J; Shillington, Donna J; Morgan, Julian K; Bull, Jonathan M; Ranero, César R (2022): Ocean bottom seismic data from the continent-ocean transition in the Deep Galicia Margin, offshore west Iberia. PANGAEA, https://doi.org/10.1594/PANGAEA.940656

Boddupalli, B., Minshull, T. A., Morgan, J., Bayrakci, G., & Klaeschen, D. (2021). Comparison of two- and three-dimensional full waveform inversion imaging using wide-angle seismic data from the Deep Galicia Margin. *Geophysical Journal International*. https://doi.org/10.1093/gji/ggab164

Boillot, G., & Winterer, E. L. (1988). *DRILLING ON THE GALICIA MARGIN: RETROSPECT AND PROSPECT*. *Proceedings of the Ocean Drilling Program, Scientific Results*.

Boillot, G., Feraud, G., Recq, M., & Girardeau, J. (1989). Undercrusting by serpentinite beneath rifted margins. *Nature, 341*, 523-525.

Boillot, G., Grimaud, S., Mauffret, A., Mougenot, D., Kornprobst, J., Mergoil-Daniel, J. and Torrent, G. (1980). Ocean--continent boundary of the Iberian margin: a serpentinite diapir west of the Galicia Bank. Earth Planet. Sci. Lett., 48: 23--34.

Brune, S. (2016). Rifts and rifted margins: A review of geodynamic processes and natural hazards. Plate Boundaries and Natural Hazards, 219, 11-37.

Brune, S., Heine, C., Clift, P. D., & Pérez-Gussinyé, M. (2017). Rifted margin architecture and crustal rheology: Reviewing Iberia-Newfoundland, Central South Atlantic, and South China Sea. *Marine and Petroleum Geology*, *79*, 257–281. https://doi.org/10.1016/j.marpetgeo.2016.10.018

Brune, S., Heine, C., Pérez-Gussinyé, M., & Sobolev, S. V. (2014). Rift migration explains continental margin asymmetry and crustal hyper-extension. *Nature Communications*, *5*, 1–9. https://doi.org/10.1038/ncomms5014

Buck, W. R. (1988). Flexural Rotation of Normal Faults, *7*(5), 959–973.

Chian, D., Louden, K. E., Minshull, T. A., & Whitmarsh, R. B. (1999). Deep structure of the ocean-continent transition in the southern Iberia Abyssal Plain from seismic refraction profiles: Ocean Drilling Program (Legs 149 and 173) transect. *Journal of Geophysical Research: Solid Earth*, *104*(B4), 7443–7462. https://doi.org/10.1029/1999jb900004

Christensen, N. I., & Mooney, W. D. (1995). Seismic velocity structure and composition of the continental crust: a global view. *Journal of Geophysical Research*, *100*(B6), 9761–9788. https://doi.org/10.1029/95JB00259

Christensen, Nikolas I. (2004). Serpentinites, peridotites, and seismology. *International Geology Review*, *46*(9), 795–816. https://doi.org/10.2747/0020-6814.46.9.795

De Charpal, O., Guennoc, P., Montadert, L., & Roberts, D. G. (1978). Rifting, crustal attenuation and subsidence in the Bay of Biscay. *Nature*, *275*(5682), 706–711. https://doi.org/10.1038/275706a0

Franke, D. (2013, May). Rifting, lithosphere breakup and volcanism: Comparison of magma-poor and volcanic rifted margins. *Marine and Petroleum Geology*. https://doi.org/10.1016/j.marpetgeo.2012.11.003

Germanovich, L. N., Genc, G., Lowell, R. P., & Rona, P. A. (2012). Deformation and surface uplift associated with serpentinization at mid-ocean ridges and subduction zones. *Journal of Geophysical Research: Solid Earth*, *117*(7), 1–23. https://doi.org/10.1029/2012JB009372

576 Graham, R. P. (1917). Origin of massive serpentine and chrysotile asbestos, Black Lake-Thetford
577 area, Quebec. *Economic Geology*, *12*(2), 154–202.

578 Hoffmann, H.-J., & Reston, T. J. (1992). Nature of the S reflector beneath the Galicia Banks rifted
579 margin: Preliminary results from prestack depth migration. *Geology*, *20*, 1091-1094.

580 Korenaga, J. (2017). On the extent of mantle hydration caused by plate bending. Earth and Planetary
581 Science Letters, 457, 1-9.

582 Krawczyk, C. M., T. J. Reston, M.-O. Beslier, and G. Boillot. (1996), Evidence for detachment tectonics
583 on the Iberia Abyssal Plain margin, in Proceedings of the Ocean Drilling Program, Science Results, vol.
584 149, edited by R. Whitmarsh, D. Sawyer, and A. Klaus, pp. 603–615, Ocean Drill. Program, College
585 Station, Tex.

586 Leythäuser, T., Reston, T. J., & Minshull, T. A. (2005). Waveform inversion of the S reflector west of
587 Spain: Fine structure of a detachment fault. Geophysical Research Letters.
588 https://doi.org/10.1029/2005GL024026

589 Lister, C. R. (1974). On the penetration of water into hot rock. *Geophysical Journal International*, *39*,
590 465–509.

591 Liu, Z., Pérez-Gussinyé, M., Rüpke, L., Muldashev, I. A., Minshull, T. A., & Bayrakci, G. (2022).
592 Lateral coexistence of ductile and brittle deformation shapes magma-poor distal margins: An example
593 from the West Iberia-Newfoundland margins. *Earth and Planetary Science Letters*, *578*, 117288.

594 Lymer, G., Cresswell, D. J. F., Reston, T. J., Bull, J. M., Sawyer, D. S., Morgan, J. K., et al. (2019).
595 3D development of detachment faulting during continental breakup. *Earth and Planetary Science*
596 *Letters*, *515*, 90–99. https://doi.org/10.1016/j.epsl.2019.03.018

597 Minshull, T. A., M. C. Sinha, and C. Peirce (2005), Multi-disciplinary, sub-seabed geophysical
598 imaging, Sea Tech., 46(10), 27–31.

599 Pérez-Gussinyé, M., Ranero, C. R., Reston, T. J., & Sawyer, D. (2003). Mechanisms of extension at
600 nonvolcanic margins: Evidence from the Galicia interior basin, west of Iberia. *Journal of Geophysical*
601 *Research: Solid Earth*, *108*(B5), 1–19. https://doi.org/10.1029/2001JB000901

602 Pérez-Gussinyé, Marta, & Reston, T. J. (2001). Rheological evolution during extension at
603 nonvolcanic rifted margins: Onset of serpentinization and development of detachments leading to
604 continental breakup. *Journal of Geophysical Research: Solid Earth*, *106*(B3), 3961–3975.
605 https://doi.org/10.1029/2000jb900325

606 Peron-Pinvidic, G., & Manatschal, G. (2019). Rifted margins: State of the art and future challenges.
607 Frontiers in Earth Science, 218.

Peron-Pinvidic, G., Manatschal, G., & Osmundsen, P. T. (2013). Structural comparison of archetypal Atlantic rifted margins: A review of observations and concepts. *Marine and Petroleum Geology*, *43*, 21–47. https://doi.org/10.1016/j.marpetgeo.2013.02.002

Ranero, C. R., & Pérez-Gussinyé, M. (2010). Sequential faulting explains the asymmetry and extension discrepancy of conjugate margins. *Nature*, *468*(7321), 294–299. https://doi.org/10.1038/nature09520

Reston, T. J. (2005). Polyphase faulting during the development of the west Galicia rifted margin. *Earth and Planetary Science Letters*, *237*(3–4), 561–576. https://doi.org/10.1016/j.epsl.2005.06.019

Reston, T. J. (2005). Polyphase faulting during the development of the west Galicia rifted margin. Earth and Planetary Science Letters, 237(3-4), 561-576.

Reston, T. J. (2009). The structure, evolution and symmetry of the magma-poor rifted margins of the North and Central Atlantic: A synthesis. Tectonophysics, 468(1-4), 6-27.Whitmarsh, R. B., Manatschal, G., & Minshull, T. A. (2001). Evolution of magma-poor continental margins from rifting to seafloor spreading. *Nature*, *413*(6852), 150–154. https://doi.org/10.1038/35093085

Reston, T. J., & Mcdermott, K. (2014). An assessment of the cause of the "extension discrepancy" with reference to the west Galicia margin. *Basin Research*, *26*(1). https://doi.org/10.1111/bre.12042

Reston, T. J., Booth-Rea, G., Leythaeuser, T., Sawyer, D., Klaeschen, D., & Long, C. (2007). Movement along a low-angle normal fault: The S reflector west of Spain. *Geochemistry, Geophysics, Geosystems*, *8*(6), 1–14. https://doi.org/10.1029/2006GC001437

Reston, T. J., Krawczyk, C. M., & Klaeschen, D. (1996). The S reflector west of Galicia (Spain): Evidence from prestack depth migration for detachment faulting during continental breakup. *Journal of Geophysical Research: Solid Earth*, *101*(B4), 8075–8091. https://doi.org/10.1029/95JB03466

Reston, T., & Mcdermott, K. (2014). An assessment of the cause of the "extension discrepancy" with reference to the west Galicia margin. *Basin Research*. https://doi.org/10.1111/bre.12042

Rüpke, L. H., & Hasenclever, J. (2017). Global rates of mantle serpentinization and H2 production at oceanic transform faults in 3-D geodynamic models. Geophysical Research Letters, 44(13), 6726-6734.

Schuba, C Nur, Gray, G. G., Morgan, J. K., Sawyer, D. S., Shillington, D. J., Reston, T. J., et al. (2018). A low-angle detachment fault revealed: Three-dimensional images of the S-reflector fault zone along the Galicia passive margin. *Earth and Planetary Science Letters*, *492*, 232–238. https://doi.org/10.1016/j.epsl.2018.04.012

638 Sibuet, J.-C. (1992). New constraints on the formation of the non-volcanic continental Galicia-
639 Flemish Cap conjugate margins. *Journal of the Geological Society*, *149*(5), 829–840.
640 https://doi.org/10.1144/gsjgs.149.5.0829

641 Watremez, L., Prada, M., Minshull, T., O'Reilly, B., Chen, C., Reston, T., et al. (2018). Deep
642 structure of the Porcupine Basin from wide-angle seismic data. *Petroleum Geology Conference*
643 *Proceedings*, *8*(1), 199–209. https://doi.org/10.1144/PGC8.26

644 Whitmarsh, R. B., Dean, S. M., Minshull, T. A., & Tompkins, M. (2000). Tectonic implications of
645 exposure of lower continental crust beneath the Iberia Abyssal Plain, Northeast Atlantic Ocean:
646 Geophysical evidence. *Tectonics*, *19*(5), 919–942.

647